Probing and controlling autoionization dynamics of atoms with attosecond light pulses

Wei-Chun Chu and C. D. Lin

Abstract The time evolution of an autoionizing atomic system is studied theoretically in the presence of a moderately intense dressing laser pulse. We first examine how an autoionizing wave packet evolves in time in the absence of an external field, and take the single $2pns(^1P)$ resonances in beryllium as examples. Alternatively, we study the electron dynamics where an attosecond extreme ultraviolet (XUV) pulse excites two autoionizing states in the presence of a strong time-delayed coupling infrared (IR) laser pulse. The IR can be viewed as a probe to extract or a control to modify the autoionization dynamics. The photoelectron and photoabsorption spectra are calculated for various time delays between the XUV and the IR pulses, and the results are compared with the available experiments. Finally, simulation of the coupled $2s2p(^1P)$ and $2s^2(^1S)$ resonances in helium shows substantial spectral modifications by the dressing field parameters. Its analogy to electromagnetically induced transparency in the time domain is discussed.

1 Introduction

The recent developments in attosecond light pulses have brought numerous applications in measuring and controlling electron dynamics in the past decade [1, 2, 3]. Single attosecond pulses (SAPs), first realized in 2001 [4], have been used in the experiments in atomic [5, 6, 7], molecular [8, 9], and condensed systems [10]. These pulses, produced by the high-order harmonic generation (HHG) process of atoms in an intense infrared (IR) light source usually cover up to the extreme ultraviolet

Wei-Chun Chu
J. R. Macdonald Laboratory, Department of Physics, Kansas State University, Manhattan, Kansas 66506, USA, e-mail: wcchu@phys.ksu.edu

C. D. Lin
J. R. Macdonald Laboratory, Department of Physics, Kansas State University, Manhattan, Kansas 66506, USA, e-mail: cdlin@phys.ksu.edu

(XUV) range and last for as short as a hundred attoseconds. With such energy and time scales, these attosecond pulses are ideal for the study of autoionization dynamics in an atomic or molecular system.

The wave packet of one or several autoionizing states (AISs) initiated by a short XUV pulse evolves in time. This evolution in the absence of an external field after the pump has been formulated and analyzed previously [11, 12, 13, 14]. We develop a simple analytical model for the freely propagating wave packet, where the atomic structure is conveniently given by a set of parameters. Taking the $2p4s(^1P)$ resonance in beryllium as an example, the photoelectrons distributed in energy and in space are calculated and analyzed until the end of the autoionization when the energy distribution converges to the well-known Fano lineshape. This process takes about ten times the decay lifetime of the AIS. Our model is further generalized for a series of resonances, demonstrated by the $2pns(^1P)$ series in beryllium. To probe the evolution of the wave packet, a pump-probe scheme with two attosecond XUV pulses is proposed; however, the scheme is currently impractical since the required light sources are still unavailable.

Alternatively, autoionizing systems have been studied in the XUV-plus-IR pump-probe scheme theoretically [15, 16, 17, 18] and experimentally [19] with long pulses–typically tens of femtoseconds to picoseconds, which are longer than the resonance lifetimes. In these cases, the total ionization yield versus the photon energy of the probe pulse is measured. Contrary to using long pulses, very recently the decay of the AIS has been measured in the broadband spectra using an XUV SAP and a femtosecond IR [20, 21]. In order to treat the accurate wave packet dynamics in the broadband lights, which has not been done before theoretically, in Sec. 3 and 4, we calculate the electron and absorption spectra, respectively, with the analyses and comparisons to the available experiments.

In the XUV-plus-IR experiments, a considerably intense IR should be viewed more rigorously as a modification of the dynamics rather than just a probe. In this aspect, in the last part of this Chapter, we calculate the $2s2p(^1P)$ and $2s^2(^1S)$ AISs coupled by a dressing laser, and discuss the dynamics manipulated by the tunable dressing pulse. When the dressing field is long, the comprehensive controlling scheme is reduced to the electromagnetically induced transparency (EIT) [22, 23] condition, which is at the heart of many current researches in optical control [24, 25, 26, 27]. While the dynamics in our model system would provide a real attosecond electron control, the EIT-like light modification therein would also open a platform for optical control when incorporated with macroscopic effects in the medium.

In this Chapter, as a general rule, atomic units (a.u.) are used for the model descriptions in Sec. 2, 3, and 4; electron Volts (eV) and femtoseconds (fs) or attoseconds (as) are used in energy and in time, respectively, for the applications or the simulations, unless otherwise specified. The pulse duration is defined by the full width at half maximum (FWHM) of the intensity.

2 Evolution of an isolated autoionizing state

Atomic autoionization typically occurs in a few to tens of femtoseconds and is one of the fastest many-electron correlation phenomena. It has been observed in frequency domain for decades via photoionization using synchrotron radiations, where the resonance features can be characterized by Fano's configuration interaction (CI) theory [28]. Tremendous improvements in experiments and theories in the past few decades have matured this research field [29, 30, 31]. Recently, with the advances in ultrafast technologies, autoionization dynamics measured in the time domain are beginning to appear with attosecond light pulses [20, 21]. It is thus of interest to formulate theories that would help to understand the evolution of an autoionizing wave packet [32].

2.1 Time evolution of an autoionizing wave packet

Assume that an ultrashort light pulse pumps an atomic system from the ground state to an AIS. After the pulse is over, an isolated autoionizing wave packet is consisting of a bound state $|\alpha\rangle$ and its background continuum $|\beta_E\rangle$. The wave packet can be written either in the configuration basis as

$$|\Psi_{ex}(t)\rangle = d_\alpha(t)|\alpha\rangle + \int d_E(t)|\beta_E\rangle dE, \tag{1}$$

or in the eigenstate basis ($|\psi_E\rangle$) as

$$|\Psi_{ex}(t)\rangle = \int c_E e^{-iEt}|\psi_E\rangle dE. \tag{2}$$

Note that the notations c and d are for eigenstates and for configurations, respectively. Applying Fano's theory of configuration interaction [28], for the atomic Hamiltonian near the resonance given by

$$\begin{aligned} \langle\alpha|H|\alpha\rangle &= E_r, \\ \langle\beta_E|H|\alpha\rangle &= V_E, \\ \langle\beta_{E'}|H|\beta_E\rangle &= E\,\delta(E'-E), \end{aligned} \tag{3}$$

the eigenstates in the form of

$$|\psi_E\rangle = a_E|\alpha\rangle + \int b_{EE'}|\beta_{E'}\rangle dE', \tag{4}$$

are solved, i.e., a_E and $b_{EE'}$ are obtained. Note that the continuum states $|\beta_E\rangle$ are assume to be real standing waves by convention so that V_E is real. By the further approximation that $|\beta_E\rangle$ differ only slightly across the resonance, the resonance width and the q-parameters, defined by

$$\Gamma \equiv 2\pi V^2, \tag{5}$$

$$q \equiv \left.\frac{\langle\alpha|T|i\rangle}{\pi V\langle\beta_E|T|i\rangle}\right|_{E=E_r}, \tag{6}$$

are taken as constants estimated at E_r.

With Eq. (4), the forms in Eq. (1) and in Eq. (2) are equated to give

$$d_\alpha(t) = \left[d_\alpha^{(0)} e^{-\frac{\Gamma}{2}t} + \int d_E^{(0)} g_E(t) dE\right] e^{-iE_r t}, \tag{7}$$

$$d_E(t) = \left[d_\alpha^{(0)} g_E(t) + \int d_{E'}^{(0)} f_{EE'}(t) dE'\right] e^{-iE_r t} + d_E^{(0)} e^{-iEt}, \tag{8}$$

where $d_\alpha^{(0)} \equiv \langle\alpha|\Psi_{ex}(0)\rangle = \langle\alpha|T|i\rangle$ and $d_E^{(0)} \equiv \langle\beta_E|\Psi_{ex}(0)\rangle = \langle\beta_E|T|i\rangle$ are the initial values of the bound and continuum coefficients, respectively, for initial (ground) state $|i\rangle$ and pump transition operator T, and $g_E(t)$ and $f_{EE'}(t)$ are defined by

$$g_E(t) \equiv \frac{V}{E - E_r + i\Gamma/2}\left[e^{-i(E-E_r)t} - e^{-\frac{\Gamma}{2}t}\right], \tag{9}$$

$$f_{EE'}(t) \equiv \frac{V}{E - E'}\left[g_E(t) - g_{E'}(t)\right]. \tag{10}$$

The evolution of $\Psi_{ex}(t)$ is uniquely determined once the Fano parameters and the initial values $d_\alpha^{(0)}$ and $d_E^{(0)}$, taken at the end of the pump pulse, are given.

The analytical form of the wave packet has a time scale of $1/\Gamma$ and an energy scale of Γ. In other words, we have arrived in a universal behavior of the autoionizing wave packet by scaling the time and the energy with respect to Γ. This will be shown in more details in the example in Sec. 2.2. For an AIS that can be treated independently, this model evaluates its evolution efficiently by importing the Fano parameters without any tedious numerical efforts. However, we have to limit the pump to be weak and short such that it is a one photon process and that the decay starts mainly after the pump, which are not necessary in the *ab initio* calculations.

For an autoionization process initiated by a broadband pulse, the "electron profile", or simply "profile", of the resonance is defined by the projection of wave packet onto the continuum waves of momentum $\mathbf{k}$ at any given time during the process. The energy-normalized continuum waves are

$$\psi_{\mathbf{k}}(\mathbf{r}) = \sqrt{\frac{2}{\pi k}}\frac{1}{r}\sum_{lm} i^l e^{i\eta_l} u_l(kr) Y_l^m(\hat{r}) Y_l^{m*}(\hat{k}), \tag{11}$$

where $u_l(kr)$ are taken as real standing waves for consistency with $|\beta_E\rangle$. Since the current study concerns only one continuum channel, or one partial wave, we focus on the total energy distribution by integrating the projection over all directions. For the wavefunction in Eq. (1), the profile is a function of energy and time given by

$$P_E(t) = |d_E(t)|^2. \tag{12}$$

As $t \to \infty$, the bound state decays to zero, and $P_E(t)$ converges to the familiar Fano lineshape. The total probability of the wave packet in Eq. (1) is normalized to 1 since the ground state is not needed after the pump ends. The expression of the model so far is for a single resonance. However, for a broadband SAP that covers multiple resonances, the model is further generalized to deal with a Rydberg series of resonances embedded in a background continuum by neglecting the higher-order interactions between the AISs.

2.2 Applications to the 2p4s resonance in beryllium

To fully comprehend the short-time behavior of the wave packet, we look at the photoelectron profile $P_E(t)$ in energy domain and the associated electron density in space. By assuming the pump pulse is perturbative and in a Gaussian envelope shorter than the autoionization time, the initial continuum distribution is given by a Gaussian function whose bandwidth is inversely proportional to the pulse duration. This distribution, consolidated with the q-parameter, determines the initial coefficients $d_\alpha^{(0)}$ and $d_E^{(0)}$. Thus, for given pump parameters and given Fano parameters, the wave packet can be calculated exactly. In the following, we take the isolated $2p4s(^1P)$ resonance and the $2pns(^1P)$ series in the $2s\varepsilon p(^1P)$ background continuum in neutral beryllium as examples. The Fano parameters are taken from the earlier calculation [33] and the experiment [34].

Following the expression in Eq. (1), the isolated $2p4s$ autoionizing wave packet can be projected onto the two-electron coordinate space as

$$\Psi_{ex}(\mathbf{r}_1,\mathbf{r}_2;t) = d_\alpha(t)\phi_\alpha(\mathbf{r}_1,\mathbf{r}_2) + \int d_E(t)\phi_E(\mathbf{r}_1,\mathbf{r}_2)dE, \tag{13}$$

where we have assumed only two active electrons. The bound-state configuration $\phi_\alpha(\mathbf{r}_1,\mathbf{r}_2)$ is composed by the $2p$ and $4s$ orbitals, and the continuum-state configuration $\phi_E(\mathbf{r}_1,\mathbf{r}_2)$ is composed by the $2s$ orbital and the εp partial wave, where both configurations are symmetrized between $\mathbf{r}_1$ and $\mathbf{r}_2$. The one-electron radial density for the wave packet is defined by

$$\rho(r,t) = \int\int\int |\Psi_{ex}(\mathbf{r},\mathbf{r}';t)|^2 r^2 r'^2 d\Omega d\Omega' dr'. \tag{14}$$

Figure 1 shows the time evolution of the $2p4s$ autoionizing wave packet in beryllium initiated by an 1.5-fs XUV pump. The time scale of the plot is relative to the decay lifetime $T = 3.78$ fs. The 1.2-eV finite bandwidth confines the overall energy distribution throughout the evolution up to $t = 10T$. The profile at $t = T$ is at the halfway between the initial Gaussian function and the final form. After that, the evolution slows down until the profile reaches its final Fano shape at roughly $10T$.

The radial electron density $\rho(r,t)$ at short times and at long times are shown in Fig. 1(b) and 1(c) respectively. At the start of the process, the $2p4s$ bound-state

wavefunction is dominant, as shown by the $t = 0$ curve. Then, the ionized electrons grow and move in a bulk to around 40 a.u. at $0.5T$ and to around 80 a.u. at T, and in the meantime, the bound state component drops. In the $0 < r < 5$ a.u. region, the sharp rising of the density means the increase of the $2s$ electrons in the $2s\varepsilon p$ configuration. As the time passes $10T$, in Fig. 1(c), the photoelectrons move outwardly with a constant average speed, but they spread wider in the r-space. This is consistent with the stabilized energy profile for $t \geq 10T$ in Fig. 1(a) where the electrons congregate around 2.5 eV and 3.2 eV. These two groups of electrons move farther away from each other in space. Considering $P(E,t)$ and $\rho(r,t)$ together assists us to "visualize" the whole autoionization process.

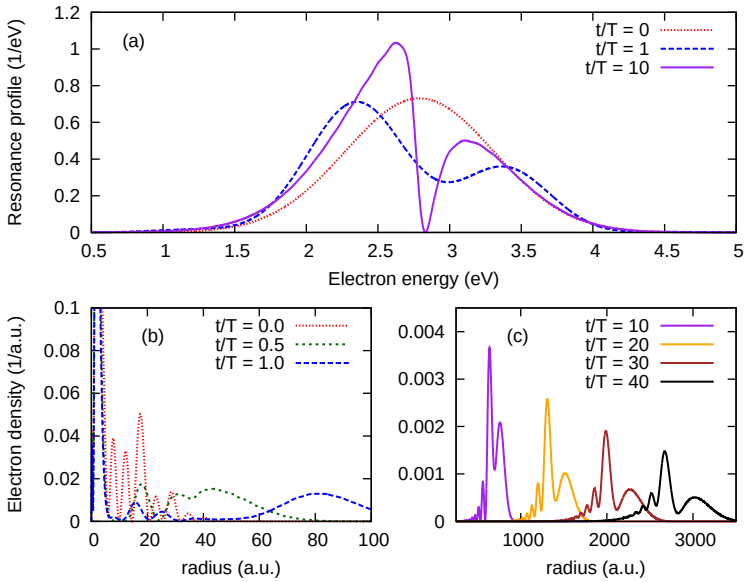

Fig. 1 Time evolution of the wave packet describing the autoionization of $2p4s$ in Be, initiated by an 1.5 fs XUV pulse centered at the resonance energy. (a) Resonance profiles at $t = 0$, T, and $10T$. The radial density of the autoionized electrons in coordinate space is shown in (b) for short times and in (c) for long times. The time is scaled by the lifetime of the resonance, $T = 3.78$ fs.

For the generalized model for multiple resonances, in Fig. 2, we show the electron profile of the $2pns$ series at different times, initiated by an 1-fs pulse centered at 2.5 eV. At $t = 0$, the curve represents the directly ionized electrons, whose distribution is proportional to the light spectrum. Then, the bound states start to decay. The decay lifetimes for the $n = 3$, 4, and 5 resonances, at $E_r = 1.6$, 2.8, and 3.3 eV, are 1.3, 3.6, and 7.9 fs, respectively. With these specific lifetimes, as seen in the 2.5- and 5-fs curves, the resonances build up at different speeds. By 100 fs, the profile of the series shows all the resonance shapes quite clearly up to $2p9s$, whose decay lifetime is 55 fs. The experimental photoionization spectrum measured by synchrotron is

shown for reference. The experimental signals are rescaled in our plot range. Other than the background curvature determined by the pulse bandwidth, our model agrees well with the experiment. In particular, the $2p4s$ resonance, which sits at the center of the pulse, is almost unaffected by the pulse profile.

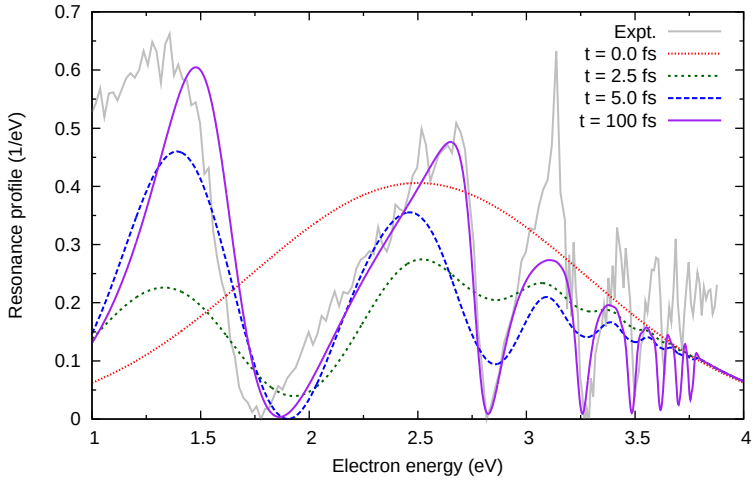

Fig. 2 Comparison of $2pns$ resonance series obtained from synchrotron radiation measurement [16] (light gray solid curve) with the simulated time-dependent profile of the same series at $t = 0$, 2.5, 5, and 100 fs, populated by an 1-fs pulse (bandwidth is 1.8 eV) centered at 2.5 eV above the threshold. The resonances for $n = 3$-9 are included in the model. The resonance parameters are generated by quantum defect $\mu = 0.6$, $\Gamma\nu^3 = 7.1$ eV where ν=n-μ, and $q = -0.8$. The experimental data has been scaled to match the calculated $2p4s$ peak at $t = 100$ fs.

We have developed and tested a simple analytical model for the dynamics of one or a series of autoionizing states that evolve freely after populated by an SAP. In an actual measurement, the retrieval of the time-dependent electron profile that evolves in only a few femtoseconds is desirable. To this end, we propose a pump-probe scheme [32] where two XUV SAPs are employed. Taking the $2p4s$ resonance analyzed above as an example, the scheme works in the following way. After the pump, a time-delayed 40-eV XUV SAP is applied to the system, which ionizes the $2s$ electron in the Be^+ ion core. These ionized electrons, at 22 eV, are much more energetic than the autoionized electrons at 2.5 eV. In other words, the probe transforms a small fraction of the system to the doubly charged Be^{2+} ions plus the 2.5- and 22-eV electrons. In the meantime, most atoms are not influenced by the probe; they only finish the autoionization process by producing the Be^+ ions and the 2.5-eV autoionized electrons that reach the ideal Fano shape. To single out the profile at the time of the probe, the detector has to record the electron signals in coincidence with the Be^{2+} ions. Theoretically, this scheme enables us to trace the fast-changing photoelectron distribution in the time scale of the pulse durations.

However, the required light sources, with moderate intensity for sufficient signal strength, are not available at the present time.

3 Electron dynamics of laser-coupled autoionizing states

The XUV-plus-IR pump-probe scheme has been utilized to study electron dynamics in various systems since the first such experiment a decade ago [5]. Typically, this setup is prepared by the HHG, and the IR is much stronger than the XUV. Thus, while the IR is designed to "probe" the dynamics of the system initiated by the XUV, it actually modifies the dynamics. Furthermore, in many occasions, the two pulses are overlapped for better signal strength, where the roles of the pump and the probe are not clearly assigned. Thus, the whole process is more suitably described as the photoionization of a system dressed by a laser pulse.

In such a scheme, photoionization of a system in the structureless region above the ionization threshold is carried out in a number of experiments [4, 35, 36, 37], and modeled by the "streaking" theory based on the strong-field approximation (SFA) [38]. If the region contains an AIS, the theory is modified to include the bound-state structure [39], which has been employed in the recent experiment in helium [21]. The simulation therein only considers the ionization of the $2s2p(^1P)$ AIS but not its coupling to the $2p^2(^1S)$ AIS. Such a system with two laser-coupled AISs has been formulated and studied widely for long pulses, where the photoionization spectrum is investigated by the total ionization yield versus the photon energy or detuning of the XUV [15, 16, 17, 18]. For the broadband SAP used in Ref. [21], the pulses are much shorter than the decay lifetime, or equivalently, much broader than the resonance widths, such that each XUV shot projects the whole resonance spectrum within its bandwidth. The dynamics of the photoelectron wave packet is our main concern. The model and its simulation for the experiment in Ref. [21] have been previously reported by us [40].

3.1 Model for total wavefunction

Here we model the time-dependent wavefunction of a three-level system, where the top two levels are AISs coupled by a laser pulse, and an XUV SAP pumps one of them from the ground state. The bound states and the photoelectrons with respect to the AISs are calculated.

The atomic system consists of the ground state $|g\rangle$ and two AISs, $|a\rangle$ and $|b\rangle$, embedded in the background continua $|E_1\rangle$ and $|E_2\rangle$, respectively (see Fig. 3). Note that these "states" are not atomic eigenstates, but configurations; we will discuss the wavefunction in eigenstate basis later. Suppose $|a\rangle$ is lower than $|b\rangle$ in energy, i.e., $E_a < E_b$, for the model description. An XUV pulse couples $|g\rangle$ to the $|a\rangle$-$|E_1\rangle$ AIS, and a time-delayed laser pulse couples the two AISs. Here the laser is not necessar-

ily an IR, considering the energy difference between the two AISs; nonetheless, the laser energy is always much lower and well separated from the XUV energy. The total Hamiltonian is $H(t) = H_A + H_X(t) + H_L(t)$, where H_A is the atomic Hamiltonian, and $H_X(t)$ and $H_L(t)$ are the dipole interactions of the atomic system with the XUV and laser, respectively. The Hamiltonian of the field itself is neglected. Both pulses are assumed to be in the form of $E(t) = F(t)e^{i\omega t} + F^*(t)e^{-i\omega t}$, where ω is the carrier frequency, and $F(t)$ is a cosine-square type function. Note that $F(t)$ is in general complex, but now taken as real in the calculation by neglecting the carrier-envelope phase and the chirping. The total wavefunction of this system is

$$|\Psi(t)\rangle = e^{-iE_g t}c_g(t)|g\rangle + e^{-iE_X t}\left[d_a(t)|a\rangle + \int d_{E_1}(t)|E_1\rangle dE_1\right] + e^{-iE_L t}\left[d_b(t)|b\rangle + \int d_{E_2}(t)|E_2\rangle dE_2\right], \quad (15)$$

where E_g is the ground state energy, and $E_X \equiv E_g + \omega_X$ and $E_L \equiv E_g + \omega_X + \omega_L$ represent the central energies pumped by the pulses. Since the fast-oscillating terms are factored out, the $c(t)$ and $d(t)$ coefficients are smooth functions of time.

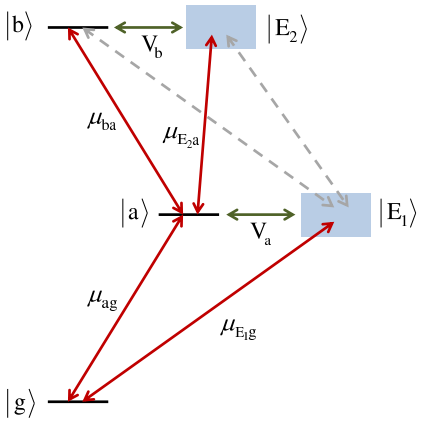

Fig. 3 Scheme of the autoionizing three-level system coupled by two ultrashort pulses. The dashed lines represent negligible transitions.

When solving the Schrödinger equation for the wavefunction, the following approximations are taken. Rotating wave approximation is applied since both pulses are nearly resonant. For the atomic systems and field conditions in our concern, the second-order electron transition between $|E_2\rangle$ and $|b\rangle$ and the free-free electron transition between $|E_1\rangle$ and $|E_2\rangle$ are disregarded. The off-diagonal terms of the Hamiltonian are thus V_a and V_b for the autoionization processes for the two AISs, $-\mu_{ag}E_X(t)$ and $-\mu_{E_1 g}E_X(t)$ for the dipole interactions for the XUV, and $-\mu_{ba}E_L(t)$ and $-\mu_{E_2 a}E_L(t)$ for the dipole interactions for the laser, where μ are dipole matrix

elements. All the V and μ are taken as constants because the continuum waves vary slightly across the resonances. The Schrödinger equation then gives the coupled equations for all the coefficients, including the continuum ones by

$$i\dot{d}_{E_1}(t) = (E_1 - E_X)d_{E_1}(t) - \mu_{E_1 g}F_X^*(t)c_g(t) + V_a d_a(t), \tag{16}$$

$$i\dot{d}_{E_2}(t) = (E_2 - E_L)d_{E_2}(t) - \mu_{E_2 a}F_L^*(t)d_a(t) + V_b d_b(t). \tag{17}$$

By adiabatic elimination of the continuum, i.e., assuming $\dot{d}_{E_1}(t) = \dot{d}_{E_2}(t) = 0$, Eqs. (16)–(17) are integrated into other coupled equations to give

$$i\dot{c}_g(t) = -i\frac{\gamma_g(t)}{2}c_g(t) - \lambda_a F_X(t)d_a(t), \tag{18}$$

$$i\dot{d}_a(t) = -\lambda_a F_X^*(t)c_g(t) - \left[\delta_X + i\frac{\Gamma_a + \gamma_a(t)}{2}\right]d_a(t) - \lambda_b F_L(t)d_b(t), \tag{19}$$

$$i\dot{d}_b(t) = -\lambda_b F_L^*(t)d_a(t) - \left[\delta_X + \delta_L + i\frac{\Gamma_b}{2}\right]d_b(t), \tag{20}$$

for the bound-state coefficients, where $\lambda_a \equiv \mu_{ag} - i\pi V_a \mu_{E_1 g}$ and $\lambda_b \equiv \mu_{ba} - i\pi V_b \mu_{E_2 a}$ are the complex dipole matrix elements combining the direct bound-bound transitions and the indirect transitions going through the continua; $\delta_X \equiv \omega_X - (E_a - E_g)$ and $\delta_L \equiv \omega_L - (E_b - E_a)$ are the detunings of the fields; and $\gamma_g(t) \equiv 2\pi|D_{E_1 g}F_X(t)|^2$ and $\gamma_a(t) \equiv 2\pi|D_{2a}F_L(t)|^2$ are the laser-induced broadenings. Note that in λ, the two μ values and V uniquely determine the q-parameter, as shown by Eq. (6). The energy independence of the continua across the resonances removes the ac Stark shifts between $|g\rangle$ and $|E_1\rangle$ and between $|a\rangle$ and $|E_2\rangle$.

By solving Eqs. (18)–(20), the bound-state part of the wavefunction in Eq. (15) is obtained. With the bound coefficients $c_g(t)$, $d_a(t)$, and $d_b(t)$, we return to Eqs. (16)–(17) for the "second iteration" of the continuum coefficients. These newly obtained continuum coefficients, opposing the divergent ones generated by the adiabatic elimination, are the final numerical functions that we apply to the total wavefunction $|\Psi(t)\rangle$ in Eq. (15). For weak fields, the system is completely described by this wavefunction. However, for strong fields, the multiphoton process or tunneling may prompt the electrons to other states or continua that are not included in the current form of $|\Psi(t)\rangle$. In the case of moderately intense laser, which is in our main concern, we have to adjust the resonance widths by adding the ionization rates estimated by the model by Ammosov, Delone, and Krainov (ADK theory) [41] or the model by Perelomov, Popov, and Terent'ev (PPT theory) [42]. In these models, the tunneling of the electrons from a bound state by an electric field is calculated at each instance. In our case, the rates are estimated with respect to the instantaneous electric field strength during the 9-fs laser. Note that while the tunneling rates correct the resonance profiles, the total probability calculated by $|\Psi(t)\rangle$ is no longer conserved.

Equivalent to Eq. (15), the wavefunction can be written in terms of atomic eigenstates as

$$|\Psi(t)\rangle = e^{-iE_g t}c_g(t)|g\rangle + e^{-iE_X t}\int c_E^a(t)|\psi_E^a\rangle dE$$

$$+ e^{-iE_L t} \int c_E^b(t)|\psi_E^a\rangle dE, \tag{21}$$

where the superscripts a and b indicate the eigenstates associated with $|a\rangle$ and $|E_1\rangle$ and with $|b\rangle$ and $|E_2\rangle$, respectively. By incorporating Fano's CI theory, the eigenstate coefficients $c_E(t)$ are given in terms of the bound and continuum coefficients by

$$c_E^a(t) = \frac{\sin\Theta_E^a}{\pi V_a} d_a(t) - (\cos\Theta_E^a - i\sin\Theta_E^a) d_{E_1}(t)|_{E_1=E}, \tag{22}$$

where

$$\Theta_E^a \equiv -\tan^{-1}\frac{\Gamma_a/2}{E-E_a} \tag{23}$$

for a, and by the same form for b where all the terms are associated with $|b\rangle$ and $|E_2\rangle$. On one hand, in the configuration basis, the coefficients evolve until both the fields and the decays are over. On the other hand, in the atomic eigenstate basis, the Hamiltonian is already diagonalized for the autoionization, i.e., the off-diagonal terms are only the dipole transition terms, and the coefficients stop changing at the end of the field. Thus, in the eigenstate basis, the calculation is necessary only up to the end of the external field, and the analytical form in Eq. (22) requires almost no additional efforts. Taking these advantages, the computational steps in the present model are first the bound-state coefficients, then the continuum-state coefficients, finally the eigenstate coefficients, where all the calculations are up to t_f at the end of the external field. The electron profiles for the two resonances are $P^a(E) = |c_E^a(t_f)|^2$ and $P^b(E) = |c_E^b(t_f)|^2$ respectively. The Fano parameters and the dipole matrix elements therein are taken from literatures or generated by preliminary calculations. Their values, involving only the atomic structures, are irrelevant to the formation of the present model.

In the analyses later in this Chapter, Rabi oscillation is at the heart of the dynamics. The generalized Rabi frequency, defined by

$$\Omega(t) \equiv \sqrt{|\mu E(t)|^2 + |\delta|^2}, \tag{24}$$

is often evaluated for the coupling strength between the states. For an ultrashort pulse, $\Omega(t)$ is only instantaneous, so the coupling over the whole pulse is illustrated by the pulse area given by

$$A \equiv \int_{-\infty}^{\infty} \Omega(t) dt. \tag{25}$$

Note that the pulse area is calculable only in a good resonance condition where $\Omega(t)$ is finite in time by neglecting δ. For a π-pulse, i.e. $A = \pi$, the population in a two-state system is transfered from one state to the other thoroughly.

3.2 Experiment in helium

The experiment by Gilbertson *et. al.* [21] measures the photoelectrons near the $2s2p(^1P)$ resonance in helium ionized by an XUV pulse with a time-delayed IR pulse. We simulate the spectra and compare the result with the measurement. For the XUV pulse, the central photon energy is $\omega_X = 60$ eV, the duration is $\tau_X = 100$ as, and the intensity is weak (perturbative). For the time-delayed IR, the wavelength is $\lambda_L = 780$ nm ($\omega_L = 1.6$ eV), the duration is $\tau_L = 9$ fs, and the peak intensity is $I_L = 7 \times 10^{11}$ W/cm^2. The time delay t_0 is defined as the separation between the pulse peaks, and $t_0 > 0$ means that the XUV is earlier. With a bandwidth of about 20 eV, the XUV pumps helium from the ground state to the $2snp$ resonance series. Due to the resolution of the spectrometer, only the strongest $2s2p$ state was observed. The natural lifetime of this state is 17 fs. By measuring electron spectra vs the time delay, the autoionization dynamics of $2s2p$ in the IR field can be followed.

In Ref. [21], a simulation using the SFA model developed by Zhao and Lin [39] was used, with additional account of the ionization by the IR, where the ionization rate was estimated by the PPT theory. The simulation concluded that the intense IR depletes $2s2p$. From the time-delay spectra, the decay rate of lifetime of the state was extracted. Limited by the spectral resolution, however, modifications of the Fano resonance profiles were not reported.

Our simulation, unlike that in Ref. [21], takes the IR coupling between $2s2p$ and the $2p^2(^1S)$ resonance into account. The background continua in the measurement, for the two AISs, are $1s\varepsilon p(^1P)$ and $1s\varepsilon s(^1S)$, respectively. With the given Fano parameters for $2s2p$ [43] and for $2p^2$ [44] and the dipole matrix elements μ_{ag} [18] and μ_{ba} [45], we carry out the model calculation and fit the tunneling parameters in the PPT theory for the experiment. The calculated time-delayed electron spectra are shown in Fig. 4. For a negative delay such as $t_0 = -10$ fs, the IR appears before the XUV without affecting the autoionization, and thus the usual Fano profile appears. This Fano lineshape is shown in the figure as a reference. As t_0 increases, the IR strikes the system at the beginning of the decay of $2s2p$, and significantly depletes the $2s2p$ bound state and its autoionized electrons, resulting in minimum of the profile at $t_0 = 4$ fs shown as the lowest curve in Fig. 4(b). When t_0 increases further, passing the range specified by the horizontal bar in Fig. 4(a), the two pulses separate in time. For larger t_0, more decay of the $2s2p$ state has occurred before the IR acts on the system, and the state is less influenced by the IR, whether by tunnel ionization or by the coupling to $2p^2$. As shown in Fig. 4(c), the profile gradually revives until it reaches the original Fano profile as $t_0 \to \infty$.

Other than the overall depletion and revival, the $2s2p$ profile basically keeps the same shape. Moreover, with the 0.7 eV energy resolution of the spectrometer used in the experiment, no distinguished spectral features can be seen other than the overall depletion, by which the decay lifetime of $2s2p$ can be extracted. In Fig. 5, the signal value at the resonance peak is plotted with t_0. As explained earlier, this value drops to the minimum at about $t_0 = 5$ fs, where the IR appears when the autoionization has just started. By adjusting the parameters in the ionization rates, the model agrees with the experiment very well, except an undefined fluctuation in

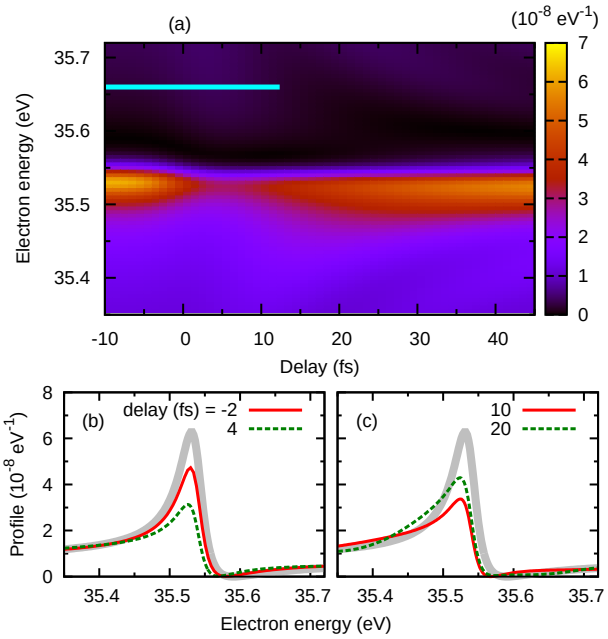

Fig. 4 Electron profile of the $2s2p$ resonance in helium. (a) Spectrogram for $t_0 = -10$ to 45 fs. The horizontal cyan bar indicates the delay range where the two pulses overlap. Particularly, the spectra are shown in (b) for $t_0 = -2$ and 4 fs, and in (c) for 10 and 20 fs. Original Fano lineshape is shown by the gray curve.

the experimental data, which has not been understood so far. For the analysis, we add two additional calculations to clarify the influence from the tunnel ionization. Without the ionization rate for $2p^2$ (W_b), the depletion is reduced to only half of that with full consideration of all the effects. This is because the binding energy of $2p^2$ (3.3 eV) is much lower than that of $2s2p$ (5.3 eV) so that $2p^2$ is ionized by the IR more easily. We now recognize that the coupling between the two states and the ionization of $2p^2$ by the IR are responsible for the depletion of the $2s2p$ profile.

Summing up the observation on the simulation and the measurement, the model produces the time-delayed photoelectron spectra of the $2s2p$ resonance that agree well with the experiment by taking the IR coupling and the tunnel ionization into account. Such a three-level photoionization by a single XUV shot has never been modeled before. The Rabi oscillation between the top two levels could potentially change the resonance shape dramatically. However, contradictory to our interest, the coupling effect is largely smeared and concealed by the tunnel ionization, where the indication of the oscillation does not stand out.

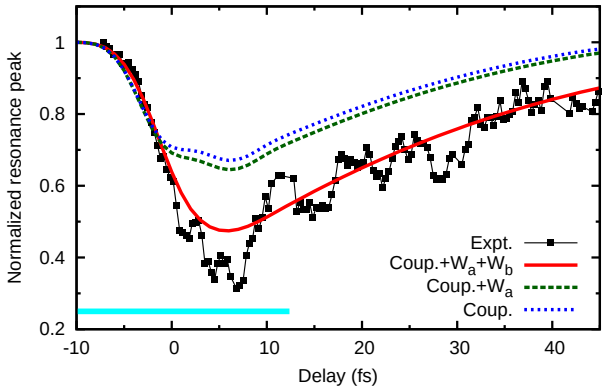

Fig. 5 Experimental and theoretical peak values of the $2s2p$ resonance profile. The cyan bar indicates the time-delay range where the two pulses overlap. Three sets of theoretical data are shown, where the labels *Coup.*, W_a, and W_b represent the coupling and the ionizations from $2s2p$ and $2p^2$, respectively. For each data set, the signal at $t_0 = -10$ fs is normalized to 1. The experimental data is shifted by 4.5 fs to the positive delay.

4 Photoabsorption of laser-coupled autoionizing states

In spectroscopy, higher spectral resolution is achieved in photoabsorption measurements than in photoelectrons. As demonstrated in Sec. 3, detailed study of a resonance profile typically requires electron energy resolution of tens to hundreds meV. In this section we formulate photoabsorption with the total wavefunction introduced in Sec. 3. A simulation is carried out and compared with the experiment by Wang *et. al.* [20]. The theory and the simulation were reported in details by us [46].

4.1 Model for photoabsorption

The formulation of photoabsorption in terms of frequency-dependent response function $\tilde{S}(\omega)$ by Gaarde *et. al.* [47] is incorporated into our model wavefunction to obtain the absorption spectra.

The total energy absorbed by an atomic system through dipole interaction with a finite light pulse is

$$\Delta U = \int_0^\infty \omega \tilde{S}(\omega) d\omega, \tag{26}$$

$$= \int_{-\infty}^\infty \frac{d\mu(t)}{dt} E(t) dt, \tag{27}$$

in the energy and time domains, respectively, where ω is the absorbed photon energy, $\mu(t)$ is the dipole moment, and $E(t)$ is the external field. The response function

$\tilde{S}(\omega)$ is the probability density of the absorption in the frequency domain, and thus is dubbed "absorption profile". It is related to the absorption cross section by

$$\tilde{\sigma}(\omega) = \frac{4\pi\alpha\omega\tilde{S}(\omega)}{\left|\tilde{E}(\omega)\right|^2}, \tag{28}$$

where α is the fine-structure constant. By the Fourier transforms of the real functions $\mu(t)$ and $E(t)$, Eqs. (26)–(27) are combined to give

$$\tilde{S}(\omega) = -2\,\mathrm{Im}\left[\tilde{\mu}(\omega)\tilde{E}^*(\omega)\right], \tag{29}$$

which is positive for absorption and negative for emission.

For the time-dependent wavefunction given by Eq. (21), $\tilde{\mu}(\omega)$ is

$$\tilde{\mu}(\omega) = \frac{1}{\sqrt{2\pi}}\int_{-\infty}^{\infty}\left[e^{i(\omega_X-\omega)t}u_X(t) + e^{i(\omega_L-\omega)t}u_L(t)\right]dt, \tag{30}$$

under the rotating wave approximation, where $u_X(t)$ and $u_L(t)$ are defined by

$$u_X(t) \equiv c_g(t)\int M_E^{ag}c_E^{a*}(t)dE, \tag{31}$$

$$u_L(t) \equiv \int c_E^a(t)\int M_{E'E}^{ba}c_{E'}^{b*}(t)dE'dE, \tag{32}$$

and M_E^{ag} and $M_{E'E}^{ba}$ are the dipole matrix elements between the eigenstates, i.e.,

$$M_E^{ag} \equiv \langle\psi_E^a|\mu|g\rangle = \frac{\sin\Theta_E^a}{\pi V_a}\mu_{ag} - \cos\Theta_E^a\mu_{E_1g}, \tag{33}$$

$$M_{E'E}^{ba} \equiv \langle\psi_{E'}^b|\mu|\psi_E^a\rangle = \left(\frac{\sin\Theta_{E'}^b}{\pi V_b}\mu_{ba} - \cos\Theta_{E'}^b\right)\frac{\sin\Theta_E^a}{\pi V_a}. \tag{34}$$

The absorption of the whole target gas is assumed to be linearly proportional to the single-atom response if the gas density is considerably low. Thus, in our simulation, the absorption and transmission profiles are simply taken as $\tilde{S}(\omega)$ and $1-\tilde{S}(\omega)$, respectively. Since the XUV and laser energies are in general widely separate, the profiles for each of the two pulse is calculated independently by taking only the necessary terms in Eqs. (30) to (34).

4.2 Experiments in argon

Recently, an experiment reported by Wang *et. al.* [20] measured the time-delayed XUV transmission spectra in argon to study its autoionization. In the report, the result was analyzed by the simulation based on an earlier model [15, 18]. It concluded that the IR significantly modified the XUV photoabsorption profile and provided a

tool for detecting and controlling autoionization. We simulate the experiment and present the comparisons with both the measurement and the calculation therein.

The 140-as SAP covers an energy range from 20 to 40 eV and populates the [Ne]$3s3p^6np(^1P)$ resonance series in argon. A time-delayed IR pulse with $\lambda_L = 750$ nm and $\tau_L = 7$ fs is applied to the system. Its intensities are 0.5 and 1 TW/cm^2 in two independent arrangements. The energy resolution of the measurement is 50 meV. Figure 6(a)–(b) shows the measured transmitted XUV profiles of the $3s3p^64p$ resonance. When the two pulses overlap, the signal is depleted, and the resonance peak roughly shifts upward in energy. As the IR lags behind the XUV, the profile gradually revives toward its Fano lineshape (note that by the convention in Ref. [20], the positive delay is on the left hand side of the plots). The result is similar to the experiment in Sec. 3. With two IR intensities, the higher one magnifies the depletion of the transmission, and a break is seen at the overlap of the two pulses.

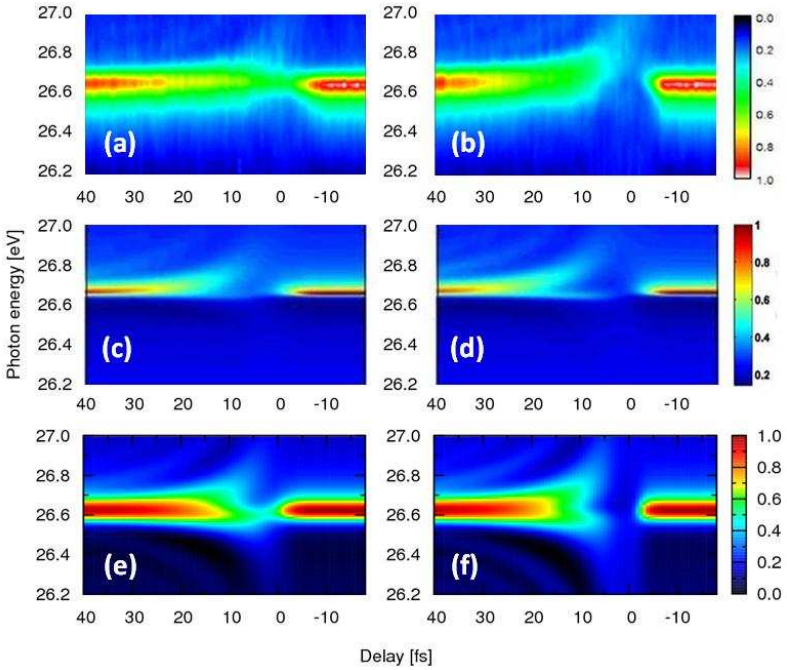

Fig. 6 Phototransmission spectrograms of the $3s3p^64d$ resonance. The left and the right panels are for 0.5 and 1 TW/cm^2 IR intensities, respectively. The top, middle, and bottom rows are the measurement and the simulation in Ref. [20], and the present simulation, respectively.

The simulation in Ref. [20] has been revised after its publication by Zhang [48] recently. The model [15, 18] calculates the total wavefunction of the system that is equivalent to the bound state part of Eq. (15) plus the preliminary continua that are used in the adiabatic elimination. This version of the wavefunction, although

unable to derive the photoelectron spectra, preserves the dipole moment quite well since the dipole moment is predominantly determined by the bound states. Zhang's simulation, plotted in Fig. 6(c)–(d), reproduces the main feature of the measurement, where the resonance profile drops abruptly from the negative delay and ascends slowly at the decay rate of the AIS to the positive delay. However, the difference between the two IR intensities is not as obvious as what the measurement shows; it seems that the simulated IR is not fully responsible for the break representing the strong AIS depletion in the measurement. Comparing our simulation in Fig. 6(e)–(f) to Zhang's simulation, the main addition of our model is the IR ionization estimated by the ADK theory, with which the spectral features near the overlap of the pulses are closer to the experiment than the previous ones, including the opening and the stronger upward curved shape of the ridge.

5 Resonant coupling in autoionizing helium

By now, we have demonstrated that the dressing laser pulse modifies the electron and absorption profiles by both the coupling between the AISs and their tunnel ionization; however, the effect of the coupling, which serves as the theme of the study, cannot be easily singled out due to the presence of tunneling. Here we propose a new XUV-plus-IR scheme in helium where $2s2p$ is coupled to the $2s^2(^1S)$ AIS resonantly with a 540-nm laser pulse. The binding energies for both AISs are high, and tunnel ionization is totally disregarded; the main dynamics is thus the Rabi oscillation between the AIS. By adjusting the coupling pulse, the resonance profiles can be manipulated more flexibly and forcefully, which would thus provide a tool for the coherent control of electrons and photons. This case study has been proposed and discussed by us for the electron dynamics [40] and photoabsorption [46].

5.1 Time-delayed electron and photoelectron spectra

In the following we keeping the field parameters used in Sec. 3 in the helium system but changing the laser wavelength to $\lambda_L = 540$ nm. The binding energies of $2s2p$ and $2s^2$ are 5.3- and 7.6-eV, respectively. The dynamics is interpreted only in terms of the coupling between the AISs.

The photoelectron profiles in the $1s\varepsilon p$ and $1s\varepsilon s$ continua, associated with $2s2p$ and $2s^2$, respectively, are calculated against the time delay, as shown in Fig 7(a)–(b). The photoabsorption profiles of the XUV and laser pulses are shown in Fig. 7(c)–(d). The four plots are in the same energy and time-delay scales, so their effects in energy and in time can be compared visually. Practically, the absorption signal is adequate only when it is comparable to the incident light signal, i.e., the total light intensity must not overwhelm the absorbed intensity along its propagation through the medium. This has not been considered in our single-atom model. Note that most

previous studies concerned only the XUV spectra that are near the resonance energy, while we include the laser spectra which contains abundant controlling features and supports the understanding of the dynamics.

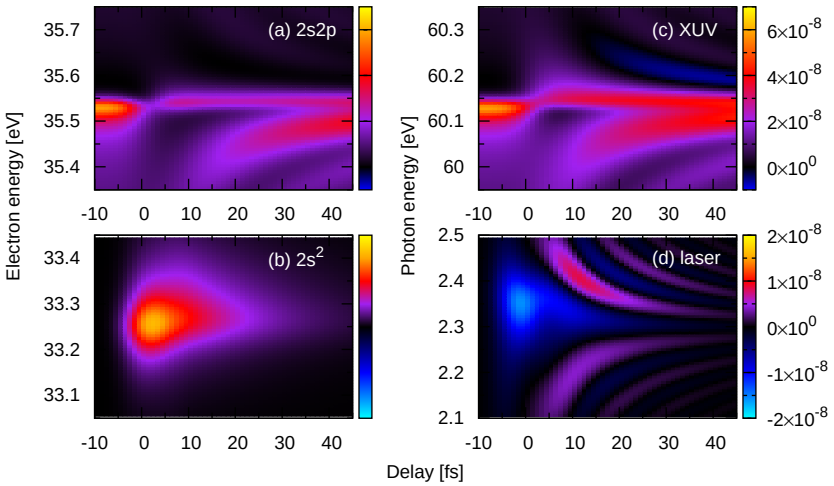

Fig. 7 Photoelectron spectrograms for the (a) $2s2p$ and (b) $2s^2$ resonances, and photoabsorption spectrograms of the (c) XUV and (d) laser pulses. The blue and cyan colors appearing in (c) and (d) represent the negative absorption, or in effect, the photoemission. The upper (lower) panels share the same color codes.

As shown in Fig. 7(a)–(b), The dramatic modifications on both electron profiles, including the enhancement, splitting, and inversion of the profile shapes, are sensitively controlled by the time delay. As the delay shifts from $t_0 = -5$ to 5 fs, the $2s2p$ profile evolves from the Fano lineshape to almost its mirror image in energy, i.e. the spectra flips upside down in Fig. 7(a) across $t_0 = 0$, in addition to the overall reduction in signal strength; the $2s^2$ profile is maximized for $0 < t_0 < 5$ fs. The pulse area of the 0.7 TW/cm^2 laser is $A = 1.6\pi$, which means that the Rabi oscillation runs 0.8 cycle between the AISs. While the laser appears right after the XUV, most electrons in $2s2p$ are driven to $2s^2$ before they take time to autoionized. Then, about half of the electrons stay in $2s^2$, while the other swing back to $2s2p$, before both states autoionize. The electrons going back to $2s2p$ change their phase by π due to the Rabi flopping, where the Fano q-parameter changes sign, resulting in the inverse image at $t_0 = 5$ fs. This mechanism is also evident in the very strong peak in Fig. 7(b). As t_0 increases, since the laser appears later in the decay of $2s2p$, more electrons are autoionized to the $2s2p$ profile before the rest are brought to $2s^2$ by the Rabi oscillation. Fewer electrons make a round trip to $2s^2$ and back to $2s2p$, and more electrons never leave $2s2p$. The population without experiencing Rabi flopping grows, which is shown in Fig. 7(a) by the lower ridge that merges upward to meet the inverse profile shape. When the time delay long passes the 17-fs decay lifetime of $2s2p$, all the electrons in $2s2p$ autoionize without ever influenced by the laser, and no electrons

show up in $2s^2$. Consequently, the $2s2p$ profile resumes the original Fano lineshape, and the $2s^2$ profile attenuates to zero.

The XUV absorption spectra are similar to the $2s2p$ electron spectra in the general appearance but with higher signals for $t_0 > 0$. This is understood where the XUV absorption is the only path for the electrons to be excited from the ground state, while the excited electrons end up in either the $2s2p$ or the $2s^2$ resonance. In other words, the XUV primarily supplies the $2s2p$ electrons, but with the existence of the laser, it also supplies the "additional" $2s^2$ electrons via the laser coupling. As for the laser absorption, as shown in Fig. 7(d), the spectra appear to be complicated. The large negative peak at 2.35 eV near $t_0 = 0$ represents the light emission corresponding to the population transfer from $2s2p$ to $2s^2$. As t_0 increases, the laser emission and absorption generate the interference pattern.

5.2 Wavelength and intensity dependence

For a given XUV light, the electron and absorption spectra are changed significantly by the dressing laser pulse. Here we examine how the laser wavelength and intensity manipulate the spectra, where the duration $\tau_L = 9$ fs and the time delay $t_0 = 15$ fs are unchanged.

In Fig. 8, the profiles are shown for peak intensities $I_L = 0.3$, 1.1, and 2.5 TW/cm^2, where the pulse areas are $A = \pi$, 2π, and 3π, respectively, with fixed $\lambda_L = 540$ nm. For $I_L = 0.3$ TW/cm^2, the π-pulse mainly brings the electrons from $2s2p$ to $2s^2$ in a one-way route; the $2s2p$ profile is strongly suppressed and the $2s^2$ profile is highly populated. As I_L proceeds to 1.1 TW/cm^2, the Rabi oscillation forms a round trip in the pulse duration. The $2s^2$ bound electrons return to $2s2p$, and the $2s^2$ profile flattens. As explained previously, the returning electrons carry a phase change of π, and the inverse q is materialized in the mirror peak image at $E \approx 35.6$ eV in Fig. 8(a). The $2s2p$ electrons that autoionize before the laser ($t_0 = 15$ fs) form the broad peak at $E = 35.45$ eV. If the intensity increases to $I_L = 2.5$ TW/cm^2, the $2s2p$ electrons move to $2s^2$ again, and the $2s2p$ profile depresses. The electrons relocating to $2s^2$ in the second Rabi cycle unite the electrons already there, and the two groups interfere to form the double-peak profile in Fig. 8(b). The same dynamics interprets the XUV profiles in Fig. 8(c), which are synonymous with the $2s2p$ electron profiles but having higher signal intensities. As for the laser spectra in Fig. 8(d), we observe that by increasing I_L, both the emission and the absorption signals heighten equally, while the profile shapes basically keep the same.

We have kept the laser in the perfect resonance condition so far, i.e., the detuning between the AISs is 0. However, since the laser duration is comparable to the decay lifetime, the bandwidth does not necessarily cover the resonance region well. Thus, the dependence of the dynamics on the detuning should be taken into account. In Fig. 9, the spectra are shown for $I_L = 0.7$ TW/cm^2 and three wavelengths $\lambda_L = 515$, 540, and 565 nm, or the photon energies of $\omega_L = 2.41$, 2.30, and 2.19 eV, respectively. Relative to the perfect resonance condition, the laser profiles in Fig. 9(d) shift

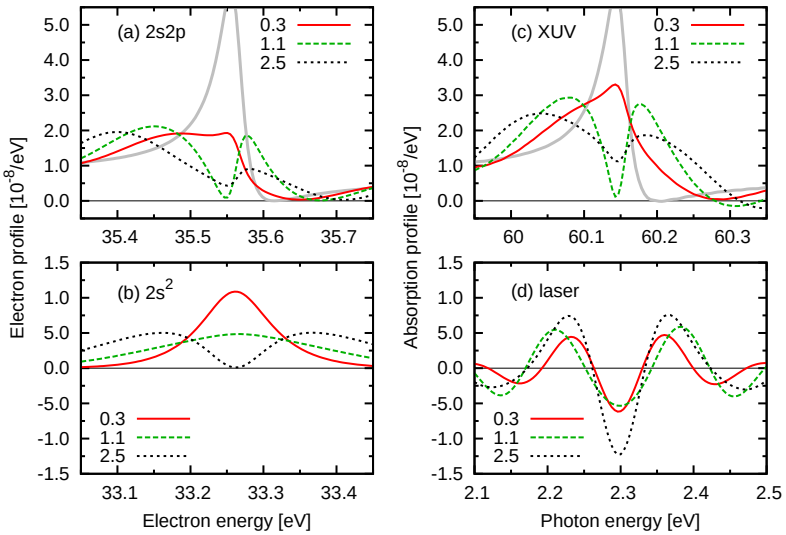

Fig. 8 Photoelectron spectra of the (a) $2s2p$ and (b) $2s^2$ resonances, and photoabsorption spectra of the (c) XUV and (d) laser pulses, for a fixed 540-nm wavelength and the intensities of 0.3, 1.1, and 2.5 TW/cm^2 of the laser. The negative signals of the absorption represent photoemission. The Fano lineshape is shown in the gray curve as a reference. The black horizontal line labels zero.

upward and downward, and the $2s^2$ profiles in Fig. 9(b) shift downward and upward (note that $2s^2$ is lower than $2s2p$ energetically) in energy, for $\omega_L = 2.41$ and 2.19 eV, respectively. Similar shifts are also seen in the $2s2p$ resonances in Fig. 9(a) and the XUV spectra in Fig. 9(c); nonetheless, the strong indications for the resonance position, at 35.55 eV electron energy or 60.15 eV photon energy, are unaffected by the laser detuning.

The analysis above show that additional to the time delay between the pulses, the laser intensity and wavelength also manipulate the outcome of the electron and photon spectra in various and sensational ways. These possibilities are provided where Rabi oscillation is the dominant mechanism, and tunnel ionization is too weak to smear the sharp contrasts produced in the spectra. The subtle changes in the spectra, such as the splitting and the flipping of the resonance shape, are measurable only when the spectrometer resolution is well beyond the energy scale of a single resonance. Considering both the resolution and efficiency, the measurement of light rather than the electrons is more suitable to study this laser manipulation on the AIS.

5.3 Dependence on pulse duration

In a pump-probe experiment, the light pulses are ideally shorter than the time scale of the dynamics being studied. This is satisfied in the current case study with an

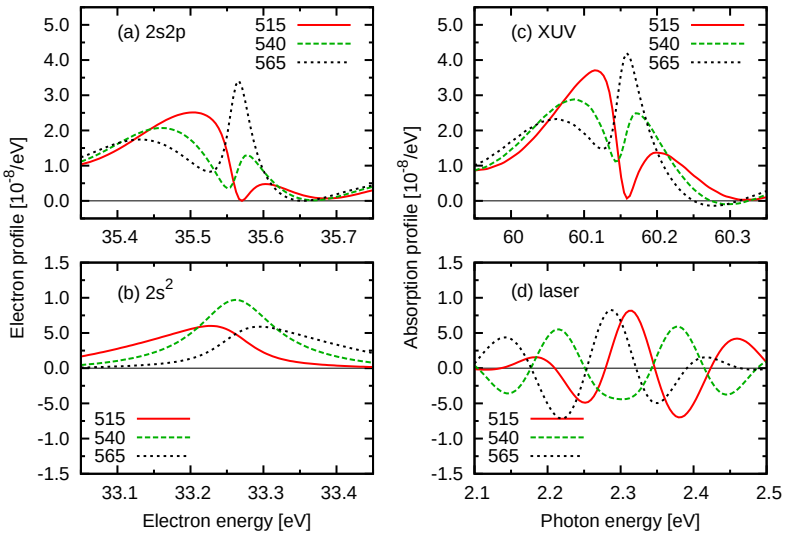

Fig. 9 As of Fig. 8 but for a fixed 0.7 TW/cm^2 laser intensity and the wavelength of 515, 540, and 565 nm.

100-as XUV and a 9-fs laser. However, in the traditional study of a dressed system, the dressing field is long, and it is to change the property of the material rather than the dynamic process. In the following, we will study the transition between short and long dressing fields using the present model.

For the two primary electron dynamics of the $2s2p$ resonance, the autoionization has a decay lifetime of 17 fs, and the Rabi oscillation between $2s2p$ and $2s^2$ has a period, evaluated at the 0.7 TW/cm^2 pulse peak, of 15.6 fs. In other words, both dynamic processes have roughly the same speed, and the 9-fs laser pulse, which is shorter than these dynamics, provides a qualified temporal resolution. In Fig. 10, we show the XUV absorption spectrograms for two longer dressing pulses, $\tau_L =$ 40 fs and 1 ps, compared with the short dressing case in Fig. 7(c). For $\tau_L = 40$ fs, many spectral features seen for $\tau_L = 9$ fs, such as the inverse q and the exponential revival of the Fano peak along t_0, disappear. The major effect is the splitting of the resonance peak between $t_0 = -10$ and 30 fs. The temporal dependence is confined by the 40-fs pulse duration, and thus the autoionization and the Rabi flopping cannot be resolved anymore. Nonetheless, by changing the delay, the magnitude of the splitting can still be controlled. For $t_L = 1$ ps, as shown in Fig. 10(b), the time delay becomes meaningless while any temporal dependence is totally washed out in the spectrogram. The system is reduced to a simple ac dressed system. The EIT condition is recovered, where an Autler-Townes doublet [49] is seen with the energy splitting of 0.26 eV.

Autler-Townes doublet is interpreted as the splitting of an energy level due to the diagonalization of the Hamiltonian when the external field contributes the coupling terms. Essentially, the $\tau_L = 40$ fs case just produces a tunable doublet that exists

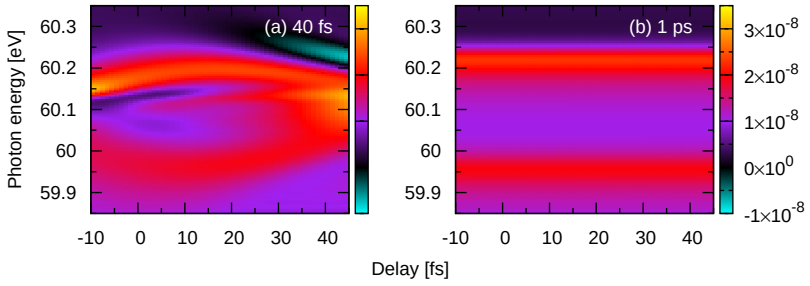

Fig. 10 Photoabsorption spectrograms for $\lambda_L = 540$ nm, $I_L = 0.7$ TW/cm^2, and the laser durations τ_L of (a) 40 fs and (b) 1 ps.

before the AISs decay, i.e., have the two states been actually bound states, the tunability would vanish. This type of temporal control of EIT has been studied in the experiment by Loh *et. al.* [45] with the $2s2p$ and $2p^2$ AISs in helium. In brief, we have demonstrated the spectral features in an autoionizing system controlled by a coupling laser pulse whose duration is compared with the autoionization and the Rabi oscillation in the system.

6 Summary

This Chapter aims to utilize the SAP to study and to control the electron and photon dynamics in an autoionizing system. The evolving wave packet for an isolated Fano resonance is calculated in energy and in space analytically by incorporating Fano's theory. For the recently available SAP-plus-IR experiments, we expand a previous three-level model to contemplate the photoelectrons promoted by the broadband XUV pulse. By including tunnel ionization, the simulated electron emission and photoabsorption of the laser-coupled AISs achieve good agreements with the measurements. To maximize the degree of manipulation in the autoionization dynamics, we propose a scheme where the Rabi oscillation between the two AISs surpasses the tunneling effect, and the electron and light spectra sensitively depend on the dressing condition. The results shows a promising ability of coherent quantum control.

Acknowledgements This work was supported in part by Chemical Sciences, Geosciences and Biosciences Division, Office of Basic Energy Sciences, Office of Science, U.S. Department of Energy. W.-C.C. greatly appreciates the discussions with Steve Gilbertson, Chang-Hua Zhang, and He Wang.

References

1. Corkum P B and Krausz F: Attosecond science. Nature Phys. **3**, 381-387 (2007)
2. Krausz F and Ivanov M: Attosecond physics. Rev. Mod. Phys. **81**, 163-234 (2009)
3. Sansone G, Poletto L, and Nisoli M: High-energy attosecond light sources. Nature Photonics **5**, 655-663 (2011)
4. Hentschel M, Kienberger R, Spielmann Ch, Reider G A, Milosevic N, Brabec T, Corkum P, Heinzmann U, Drescher M, and Krausz F: Attosecond metrology, Nature **414**, 509–513 (2001)
5. Drescher M, Hentschel M, Kienberger R, Uiberacker M, Yakovlev V, Scrinzi A, Westerwalbesloh Th, Kleineberg U, Heinzmann U, and Krausz F: Time-resolved atomic inner-shell spectroscopy. Nature **419**, 803–807 (2002)
6. Uiberacker M *et. al.*: Attosecond real-time observation of electron tunnelling in atoms. Nature **446**, 627–632 (2007)
7. Schultze M *et. al.*: Delay in photoemission. Science **328**, 1658–1662 (2010)
8. Kelkensberg F *et. al.*: Molecular dissociative ionization and wave-packet dynamics studied using two-color XUV and IR pump-probe spectroscopy. Phys. Rev. Lett. **103**, 123005 (2009)
9. Sansone G *et. al.*: Electron localization following attosecond molecular photoionization. Nature **465**, 763–766 (2010)
10. Cavalieri A L: Attosecond spectroscopy in condensed matter. Nature **449**, 1029–1032 (2007)
11. Cavalieri S and Eramo R: Time-delay spectroscopy of autoionizing resonances. Phys. Rev. A **58**, R4263–R4266 (1998)
12. Wickenhauser M, Burgdörfer J, Krausz F, and Drescher M: Time resolved Fano resonances. Phys. Rev. Lett. **94**, 023002 (2005)
13. Mercouris Th, Komninos Y, and Nicolaides C A: Time-dependent formation of the profile of the He $2s2p\ ^1P^o$ state excited by a short laser pulse. Phys. Rev. A **75**, 013407 (2007)
14. Skantzakis E, Tzallas P, Kruse J E, Kalpouzos C, Faucher O, Tsakiris G D, and Charalambidis D: Tracking autoionizing-wave-packet dynamics at the 1-fs temporal scale. Phys. Rev. Lett. **105**, 043902 (2010)
15. Lambropoulos P and Zoller P: Autoionizing states in strong laser fields. Phys. Rev. A **24**, 379–397 (1981)
16. Bachau H, Lambropoulos P, and Shakeshaft R: Theory of laser-induced transitions between autoionizing states of He. Phy. Rev. A **34**, 4785–4792 (1986)
17. Madsen L B, Schlagheck P, and Lambropoulos P: Laser-induced transitions between triply excited hollow states. Phys. Rev. Lett. **85**, 42–45 (2000)
18. Themelis S I, Lambropoulos P, and Meyer M: Ionization dynamics in double resonance involving autoionizing states in helium: the effect of pulse shapes. J. Phys. B: At. Mol. Opt. Phys. **37**, 4281–4293 (2004)
19. Karapanagioti N E, Faucher O, Shao Y L, Charalambidis D, Bachau H, and Cormier E: Observation of autoionization suppression through coherent population trapping. Phys. Rev. Lett. **74**, 2431–2434 (1995)
20. Wang H, Chini M, Chen S, Zhang C-H, He F, Cheng Y, Wu Y, Thumm U, and Chang Z: Attosecond time-resolved autoionization of argon. Phys. Rev. Lett. **105**, 143002 (2010)
21. Gilbertson S, Chini M, Feng X, Khan S, Wu Y, and Chang Z: Monitoring and controlling the electron dynamics in helium with isolated attosecond pulses. Phys. Rev. Lett. **105**, 263003 (2010)
22. Harris S E, Field J E, and Imamoglu A: Nonlinear optical processes using electromagnetically induced transparency. Phys. Rev. Lett. **64**, 1107–1110 (1990)
23. Fleischhauer M, Imamoglu A, and Marangos J P: Electromagnetically induced transparency: optics in coherent media. Rev. Mod. Phys. **77**, 633–673 (2005)
24. Lukin M D: Trapping and manipulating photon states in atomic ensembles. Rev. Mod. Phys. **75**, 457–472 (2003).
25. Glover T E, Hertlein M P, Southworth S H, Allison T K, van Tilborg J, Kanter E P, Krässig B, Varma H R, Rude B, Santra R, Belkacem A, and Young L: Controlling X-rays with light. Nature Phys. **6**, 69–74 (2010)

26. Ignesti E, Buffa R, Fini L, Sali E, Tognetti M V, and Cavalieri S: Frequency shift by optical coherent control. Phys. Rev. A **81**, 023405 (2010)
27. Ignesti E, Buffa R, Fini L, Sali E, Tognetti M V, and Cavalieri S: Controlling the spectrum of light pulses by dynamical electromagnetically induced transparency. Phys. Rev. A **83**, 053411 (2011)
28. Fano U: Effects of configuration interaction on intensities and phase shift. Phy. Rev. **124**, 1866–1878 (1961)
29. Kjeldsen H: Photoionization cross sections of atomic ions from merged-beam experiments. J. Phys. B: At. Mol. Opt. Phys. **39**, R325–R377 (2006)
30. Bilderback D H, Elleaume P, and Weckert E: Review of third and next generation synchrotron light sources. J. Phys. B: At. Mol. Opt. Phys. **38**, S773–S797 (2005)
31. West J B: Photoionization of atomic ions. J. Phys. B: At. Mol. Opt. Phys. **34**, R45R91 (2001)
32. Chu W-C and Lin C D: Theory of ultrafast autoionization dynamics of Fano resonances. Phys. Rev. A **82**, 053415 (2010)
33. Chu W-C, Zhou H-L, Hibbert A, and Manson S T: Photoionization of the Be isoelectronic sequence: total cross sections. J. Phys. B: At. Mol. Opt. Phys. **42**, 205003 (2009)
34. Wehlitz R, Lukić D, and Bluett J B: Resonance parameters of autoionizing Be $2pnl$ states. Phys. Rev. A **68**, 052708 (2003)
35. Remetter T *et. al.*: Attosecond electron wave packet interferometry. Nature Phys. **2**, 323–326 (2006)
36. Goulielmakis E, Yakovlev V S, Cavalieri A L, Uiberacker M, Pervak V, Apolonski A, Kienberger R, Kleineberg U, and Krausz F: Attosecond control and measurement: lightwave electronics. Science **317**, 769–775 (2007)
37. Mauritsson J, Johnsson P, Mansten E, Swoboda M, Ruchon T, L'Huillier A, and Schafer K J: Coherent Electron Scattering Captured by an Attosecond Quantum Stroboscope. Phys. Rev. Lett. **100**, 073003 (2008)
38. Kitzler M, Milosevic N, Scrinzi A, Krausz F, and Brabec T: Quantum theory of attosecond XUV pulse measurement by laser dressed photoionization. Phys. Rev. Lett. **88**, 173904 (2002)
39. Zhao Z X and Lin C D: Theory of laser-assisted autoionization by attosecond light pulses. Phys. Rev. A **71**, 060702R (2005)
40. Chu W-C, Zhao S-F, and Lin C D: Laser-assisted-autoionization dynamics of helium resonances with single attosecond pulses. Phys. Rev. A **84**, 033426 (2011)
41. Ammosov M V, Delone N B, and Krainov V P: Tunnel ionization of complex atoms and of atomic ions in an alternating electromagnetic field. Sov. Phys. JETP **64**, 1191–1194 (1986)
42. Perelomov A M, Popov V S, and Terent'ev M V: Ionization of Atoms in an Alternating Electric Field. Sov. Phys. JETP **23**, 924 (1966)
43. Domke M, Schulz K, Remmers G, Kaindl G, and Wintgen D: High-resolution study of $^1P^o$ double-excitation states in helium. Phys. Rev. A **53**, 1424–1438 (1996)
44. Burgers A, Wintgen D, and Rost J-M: Highly doubly excited S states of the helium atom. J. Phys. B **28**, 3163–3183 (1995)
45. Loh Z-H, Greene C H, and Leone S R: Femtosecond induced transparency and absorption in the extreme ultraviolet by coherent coupling of the He $2s2p$ ($^1P^o$) and $2p^2$ ($^1S^e$) double excitation states with 800 nm light. Chem. Phys. **350**, 7-13 (2008)
46. Chu W-C and Lin C D: Photoabsorption of attosecond XUV light pulses by two strongly laser-coupled autoionizing states. Phys. Rev. A **85**, 013409 (2012)
47. Gaarde M B, Buth C, Tate J L, and Schafer K J: Transient absorption and reshaping of ultrafast XUV light by laser-dressed helium. Phys. Rev. A **83**, 013419 (2011)
48. Zhang C-H (Private communication)
49. Autler S H and Townes C H: Stark effect in rapidly varying fields. Phys. Rev. **100**, 703–722 (1955)